Measurement of the geometric and kinematic properties of microscale breaking waves from infrared imagery using a PIV algorithm

2005 Meas. Sci. Technol. 16 1961

(http://iopscience.iop.org/0957-0233/16/10/011)

INSTITUTE OF PHYSICS PUBLISHING MEASUREMENT SCIENCE AND TECHNOLOGY

Meas. Sci. Technol. **16** (2005) 1961–1969 doi:10.1088/0957-0233/16/10/011

Measurement of the geometric and kinematic properties of microscale breaking waves from infrared imagery using a PIV algorithm

A T Jessup and K R Phadnis

Applied Physics Laboratory and Department of Mechanical Engineering, University of Washington, Seattle, WA 98105, USA

Received 27 December 2004, in final form 1 July 2005
Published 23 August 2005
Online at stacks.iop.org/MST/16/1961

Abstract

Infrared techniques have been shown to be uniquely capable of detecting and quantifying microscale breaking waves at an air–water interface. Here we extend current capabilities by developing image processing algorithms to measure the crest lengths and velocities of microbreaking waves in a laboratory wind–wave tank. The measurements are used to compute the distribution of crest lengths as a function of speed, $\Lambda(c)$, introduced by Phillips [1] as a formulation for the distribution of breaking waves. Two methods to determine the crest velocity by applying a particle imaging velocimetry (PIV) algorithm to the infrared imagery are developed and compared to a method based on tracking the centroid of the crest. The crest-PIV method is based on estimation of the velocity of crests identified using a temperature threshold. The image-PIV method is based on a velocity threshold applied to a surface velocity map obtained by using the PIV algorithm over the entire image. Both methods are used to compute the surface turnover rate, which is compared to the frequency of breaking. The methods developed demonstrate the potential for infrared imaging techniques to measure the geometric and kinematic properties of microbreaking waves and are relevant to air–sea flux studies.

Keywords: microbreaking, microscale wave breaking, infrared, PIV, image processing

(Some figures in this article are in colour only in the electronic version)

1. Introduction

The critical role of dissipation due to wave breaking in the development of the ocean surface wave field is well established. Recent theoretical work by Hara and Belcher [2] and experiments by Phillips *et al* [3] and Melville and Matusov [4] have focused on the equilibrium range theory by Phillips [1]. His theory includes relations for statistical characteristics of wave breaking in terms of the distribution of the length of breaking fronts as a function of breaking crest speed. He defines the quantity $\Lambda(c)\,\mathrm{d}c$ as the average total length of breaking fronts per unit area with crest speed between c and $c + \mathrm{d}c$. Phillips [1] gives simple expressions for the fraction of the ocean surface turned over per unit time, or the surface turnover rate, R,

$$R = \int c\Lambda(c)\,\mathrm{d}c \tag{1}$$

and for the average rate of energy loss in terms of the distribution of breaking fronts, $\varepsilon(c)$, based on laboratory experiments by Duncan [5],

$$\varepsilon(c) = bg^{-1}c^5\Lambda(c), \tag{2}$$

where b is a proportionality constant. Phillips' formulation is potentially important because the critical dynamical quantity of dissipation can be obtained from knowledge of geometric and kinematic properties alone, namely the crest

length and speed, respectively. To verify the theory, we require simultaneous measurements of the relevant geometric, kinematic and dynamic properties.

Until recently, there were no experimental techniques or data to objectively measure the geometric and kinematic quantities needed to determine $\Lambda(c)$. Phillips *et al* [3] reported the first such measurements using high-resolution radar data. Melville and Matusov [4] made measurements of $\Lambda(c)$ by applying particle imaging velocimetry (PIV) techniques to airborne video measurements. The results of both of these reports are qualitatively consistent with Phillips' theory.

Recent advances in the use of infrared (IR) imaging techniques to study breaking waves suggest that these techniques may provide the ability to both determine $\Lambda(c)$ and simultaneously provide information with which (1) and (2) can be validated for microscale breaking waves. Microscale breaking waves, or microbreaking, describe the breaking of very short gravity waves without air entrainment [6]. In general, the surface, or skin, temperature of the ocean is less than the bulk temperature immediately below by 0.1 to 0.5 °C [7]. When this cool skin is momentarily disrupted by a breaking wave, the skin temperature within the resulting turbulent wake is approximately equal to the bulk temperature. As the wake subsides, the skin layer recovers, and the skin temperature returns to its original, cooler value. Previous investigations have shown that this passive IR signature can be used to quantify wave breaking over a wide range of scales, from microbreaking [8, 9] to whitecaps [10]. The passive IR technique can provide a measure of the area of the turbulent wake produced by breaking waves. In addition, the recovery rate of the temperature in the wakes of whitecaps has been related to the turbulence intensity [10] and the fractional area coverage of microbreaking has been correlated with sub-surface PIV measurements of turbulence [11, 12]. Volino and Smith [13] used sub-surface PIV measurements of velocity to study the IR signatures of features on a evaporatively cooled water surface. More recently, Zhang and Harrison [14] applied a PIV-like technique directly to IR images of wind-generated waves to estimate surface drift speeds on the water surface.

In order to evaluate the use of IR techniques to measure $\Lambda(c)$, we developed image-processing algorithms to detect and track the fronts of breaking waves using IR imagery. Here we examine two different methods of applying a PIV algorithm to derive crest velocities and compare them with an independent centroid-tracking scheme. Our emphasis is on the development of techniques to extract the crest velocity rather than application of (1) and (2). However, the derived crest length distributions are used to compute the turnover rate from (1) and compare it to the frequency of breaking. Although the range of wind speeds is limited and only surfactant-affected data are used, the results demonstrate the potential of IR techniques for measuring the distribution of crest lengths of breaking waves. This extends the original study by Phadnis [15] by adding a modified method for estimating breaking wave characteristics.

2. Experimental setup

The data used in the algorithm development are from an experiment conducted in 2001 using the wind–wave tank in the Harris Hydraulics Laboratory at the University of Washington. The wind–wave tank is 9.2 m long and 1.2 m wide with a water depth of 0.9 m and includes an energy absorbing beach at the downstream end of the tank. Wind speed, air and bulk water temperature, and surface displacement were measured using standard techniques. Water leaving radiance was measured using a model radiance HS infrared imager (Raytheon TI Systems) with a 256 × 256 focal plane array (FPA) and a digital resolution of 12 bits. The imager is sensitive to radiation in the 3–5 μm wavelength band and the effective measurement depth, given by the optical depth in water, is approximately 10 μm. The sensitivity given by the noise equivalent temperature difference (NETD) is 25 mK. A model 2004 area-extensive blackbody (Santa Barbara Infrared) was used for calibration and FPA non-uniformity correction. The imager was mounted on top of the tank pointing upwind and aimed at the water surface from a height of approximately 1 m. The incidence angle (angle between the surface normal and the look direction) was 23° and the lens field of view was approximately 35°. The image size was approximately 65.5 cm in the vertical direction (along the tank) and 65.5 cm in the horizontal direction (across the tank). The horizontal dimension was measured at the centre of the image. Images were recorded at a rate of 120 Hz for a duration of 300 s at each wind speed.

Table 1. Wind speeds and corresponding wave parameters. Wavelength and phase speed were computed using linear wave theory based on the peak frequency of spectra in figure 1.

Wind speed (m s^{-1})	Frequency (Hz)	Wavelength (cm)	Phase speed (cm s^{-1})
6.2	4.46	7.8	35.0
8.1	3.55	12.4	44.0
9.6	3.16	15.6	49.3

The experiment was not designed for the present objectives but rather to investigate the role of microscale wave breaking in air–water gas transfer under conditions of low air–water temperature difference and variable surfactant conditions [16, 17]. The magnitude of the bulk–skin temperature difference, and therefore the thermal contrast, is enhanced by large air–water temperature differences. In general, we found that the clean surface conditions did not provide enough thermal contrast to adequately develop robust algorithms because of the low air–water temperature difference. However, the thermal contrast was significantly enhanced by the presence of surfactants. Since our primary objective was algorithm development, we chose to use the surfactant-influenced cases in order to maximize the thermal contrast in the images. The surfactant was Triton-X100 and the concentration was 1 ppm. Measurements were made at a fetch of 5.5 m for five different wind speeds from 3.8 m s^{-1} to 9.6 m s^{-1}, but only the three higher wind speeds (6.2, 8.1, 9.6 m s^{-1}) were used because at the lower wind speeds the incidence of microbreaking was small. The conditions for the wind speed and wave parameters for the three runs used are summarized in table 1 and the corresponding surface displacement spectra are shown in figure 1.

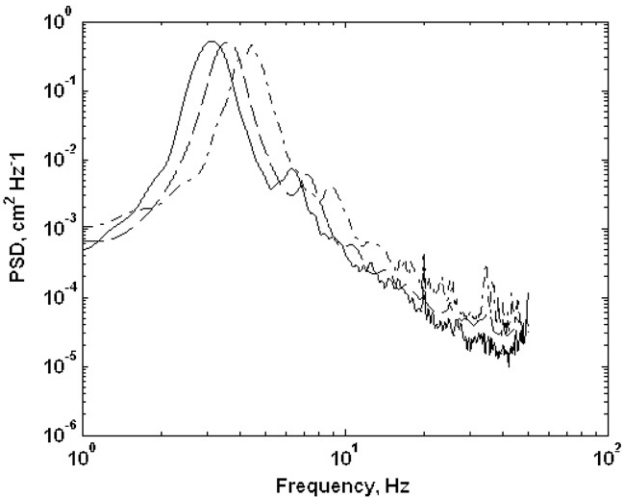

Figure 1. Surface displacement spectra for the three experimental runs used with wind speeds of 9.6 (solid line), 8.1 (dashed line) and 6.2 (dashed dotted line) m s^{-1}.

3. Crest detection

An IR image showing the typical signature of microscale breaking waves is shown in figure 2. The y-axis is oriented along the tank, pointing in the downwind direction, and the x-axis is oriented across the tank. Individual breaking events are characterized by a sharp temperature gradient corresponding to the actively breaking crest followed a well-defined warm temperature region corresponding to the wake [8, 9]. The leading edges of the microbreakers determined by the thresholding technique described below are outlined in figure 2. Finer scale temperature features due to background or residual turbulence outside the wakes and fluctuations within the wakes are also apparent in the image. The sharp gradient at the leading edge and the elevated temperature within the wakes suggest that the simplest means to detect the breaking crests is to threshold the IR image.

Zappa *et al* [9] used a thresholding technique to detect the wakes of microbreakers to estimate the fractional area coverage of microbreaking, A_B. They used a threshold given by $T_{threshold} = T_{mean} + \beta\sigma_T$, where T_{mean} is the mean image temperature, σ_T is the standard deviation of the temperature in the entire image and β is a factor used to adjust the threshold level. Zappa *et al* found that the magnitude of A_B depended on β but its functional dependence on wind speed did not vary over a relatively wide range of β. In order to use this method to consistently detect the leading edge of the wakes, we found it necessary to minimize the effect of fine-scale variations at the high and low ends of the temperature distribution of the images. This was accomplished by using a contrast enhancement operation in which all pixels above a specified high value (significantly greater than the mean) were set to that high value and all pixels below a specified low value (significantly less than the mean) were set to that low value. The high and low values used in the contrast enhancement were determined iteratively by trial and error until the thresholding scheme produced consistent results with a value of $\beta = 1$. In the process, roughly 500 images at each wind speed were overlaid with the detected contours from the thresholding. The values of the contrast enhancement parameters were varied until these overlaid contours were visually verified to identify the leading edge and the turbulent wake.

After the thresholding technique identifies the outline of the wake, the crest length is defined as the portion of the wake outline along the leading edge on the downwind side. To extract the leading edge, a local x–y coordinate system is established with the wake centroid as the origin. Then the crest was determined as the portion of the wake outline that is subtended by an angle of $\pm 90^\circ$ between the local y-axis and the local x-axis. The crests are shown superimposed on the corresponding IR image in figure 2(a). Although the

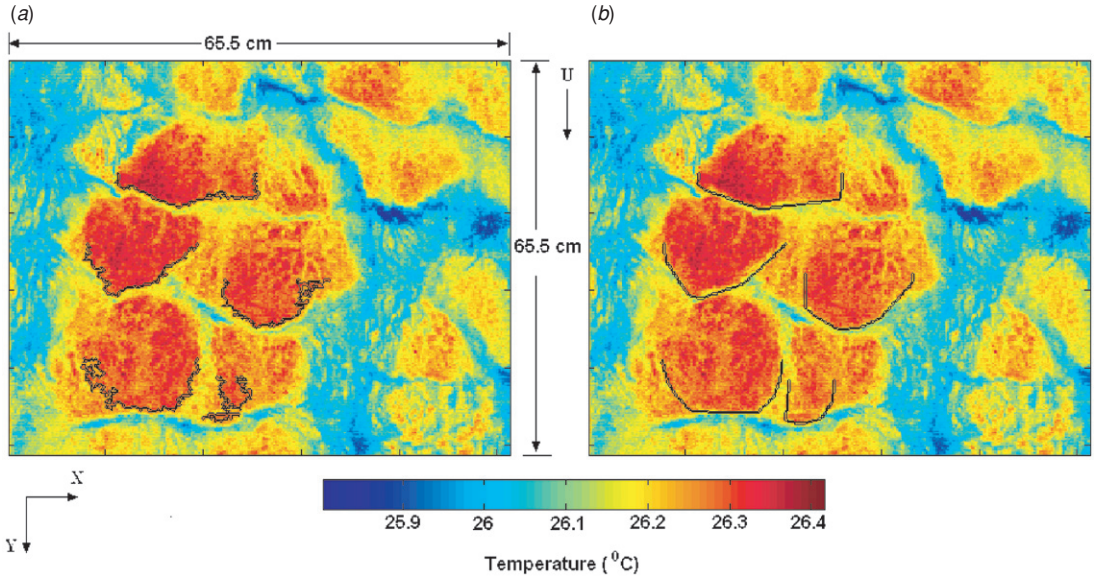

Figure 2. An IR image of microscale breaking waves at a wind speed of 9.6 m s^{-1}. (a) Contours of breaking wave fronts overlaid on the IR image detected using the crest-PIV method (a) without smoothing and (b) with smoothing.

crests determined in this manner clearly correspond to the leading edge of the wakes, they sometimes have a jagged and convoluted shape as shown in figure 2(*a*). An adverse effect of this spatial structure is that it may artificially increase the computed length of the crest. To mitigate the effect of the detailed spatial structure in the crests, a smooth curve was fitted to the crests using the smallest convex polygon as shown in figure 2(*b*). The smoothing results in less convoluted crests but also has a tendency to displace the crest from the location of the maximum temperature gradient corresponding to the leading edge of the wake.

4. Crest velocity determination

Two different methods to determine the crest velocities were evaluated by applying a standard PIV technique [18] to the IR images. The first method, called the crest-PIV method, was to apply PIV to the binary images of both the unsmoothed and smoothed crests detected using the threshold technique described above. While thresholding was verified to detect microbreaking crests, it is not able to detect all breaking crests in all images. The second method, called the image-PIV method, was to apply PIV to the entire unprocessed IR image, which resulted in a surface map of velocity over the entire image.

The PIV algorithm computes the pixel displacement between two sequential digital images using localized spatial cross correlation techniques. Two sequential images are spatially sub-sampled via an interrogation window over which the cross correlation is computed. A grid spacing parameter determines the shift in the interrogation window over the image in both horizontal and vertical directions. The size of the interrogation window was 16×16 pixels^2 and the grid spacing was 8 pixels, corresponding to a spatial resolution of 2 cm $\times$ 2 cm. Since the discernible crest displacement is very low at the image acquisition frame rate of 120 Hz, the sequence was sub-sampled by skipping every other frame, lowering the frame rate to 60 Hz. A three-point Gaussian sub-pixel peak fitting scheme was used to reduce peak locking, which is the tendency for integer displacement vector values. The PIV algorithm was first tested using artificially created binary images with all pixels equal to zeros except for horizontal lines representing artificial wave fronts with a vertical shift of several pixels between them. Displacement vectors were determined using a range of interrogation window sizes and grid spacing sizes. The displacement vectors computed using the PIV algorithm were verified to be equal to the distance between the artificial crests.

The velocity vectors computed using both the crest- and image-PIV methods for the example image in figure 2 are shown in figure 3. For the crest-PIV results in figures 3(*a*) and (*b*), most of the velocity vectors are in the downwind direction. However, there are noticeable spurious vectors, which include unreasonably large magnitudes or physically unrealistic directions. Although a peak-to-mean value ratio comparison scheme was implemented, spurious vectors were associated with the convoluted parts of the crests. By smoothing the crests, as shown in figure 3(*b*), their occurrence is reduced but not completely eliminated. This result implies that the velocity vectors are dependent on the detailed structure

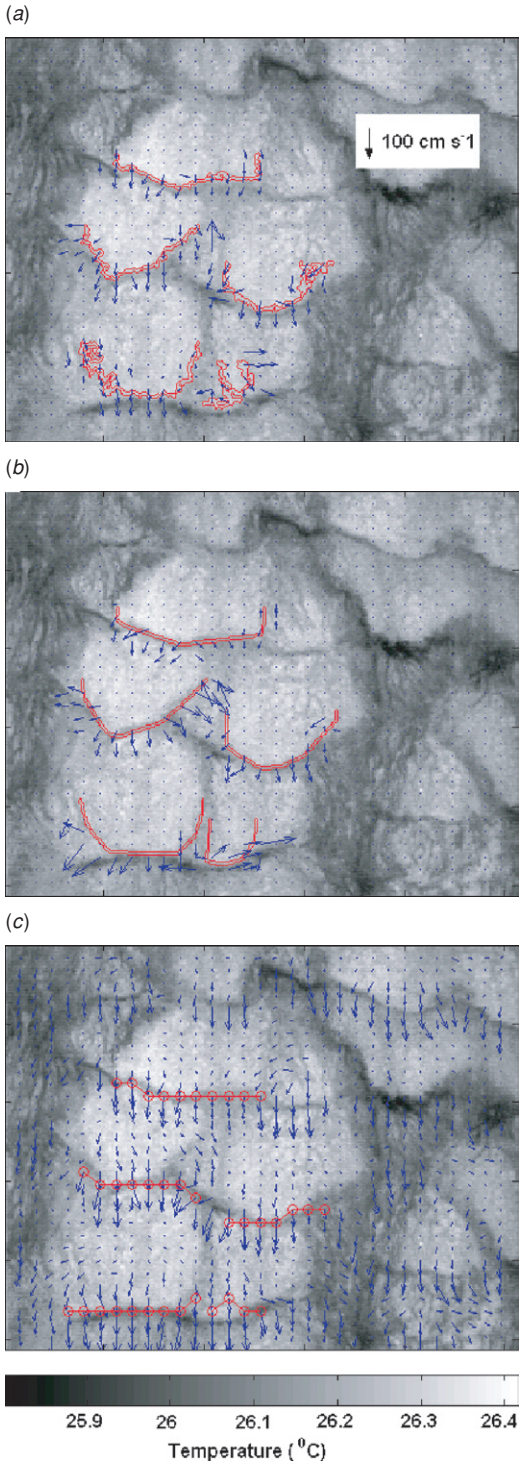

Figure 3. IR image in figure 2 overlaid with velocity vectors (blue) and detected breaking wave front contours (red) using (*a*) crest-PIV without smoothing, (*b*) crest-PIV with smoothing and (*c*) image-PIV with contours of the detected breaking wave front indicated by the red lines with circles.

of the detected crests, which can change from image to image. The remaining spurious vectors were eliminated by setting a maximum value of approximately twice the phase speed of the dominant wave and a direction limit based on the wind direction.

In addition to the variability caused by the crest structure, a further disadvantage of using a temperature threshold to detect the crest is that the threshold will likely depend on the environmental conditions that determine the bulk–skin temperature difference, such as air–water temperature difference and wind speed. These drawbacks motivated us to implement the image-PIV method, which uses a velocity rather than a temperature criterion to detect the crests. The crest speed of a breaking wave, c_{brk}, is expected to be of the order of the phase speed of the dominant wave, c_{pk}, which is significantly greater than the surface velocities of non-breaking waves and of any background turbulence. Therefore, a velocity threshold based on the magnitude of the surface velocity relative to the crest speed of the dominant wave would provide a more physically based approach than a temperature-based threshold.

The PIV algorithm described above was applied to the unprocessed IR images to produce a velocity map over each entire image, as shown in figure 3(*c*). In general, the map shows large, downwind velocities associated with the leading edges of the wakes that are comparable in magnitude to the crest velocities based on the crest-PIV method. The vectors are generally more aligned with the wave direction and do not show the same kind of erratic variability in magnitude and direction as in figures 3(*a*) and (*b*). Regions outside the wakes also show significant downwind velocities, though they appear lower and less ordered than the crest velocities. The velocities inside the wakes are relatively low and in some cases appear to show that the wakes are regions of divergent flow. The velocity map does not contain the kind of spurious vectors found in figures 3(*a*) and (*b*) near the outer edges of the crests.

Also shown in figure 3(*c*) are the crest lengths based on the image-PIV velocities. Ideally, the crest-detection scheme for the image-PIV method would be based on the velocity map alone. While we believe that this approach is reasonable and will ultimately be achieved, our preliminary efforts to develop such a scheme showed that it was beyond the scope of this study. As an intermediate approach, we chose to utilize the location of crests detected using the temperature threshold to create regions of interest (ROI) from which crest velocities and lengths from the velocity maps can be extracted. For a given crest identified by the temperature threshold method, a ROI was defined as the area within two grid points surrounding that crest. To extract the crest velocities and lengths from the image-PIV velocity maps, the ROIs were overlaid on the corresponding map of the displacement vector field. Displacement vectors coincident with each ROI were extracted and the velocity field was computed over the ROI. To identify the location of the crest based on the velocity map, the maximum y-direction velocity at each x-coordinate within the ROI was located. In this manner, the crest location and velocities were determined by the maximum downwind velocity within the ROI. The crests based on the image-PIV method in figure 3(*c*) are much straighter than both the unsmoothed and smoothed crests based on the temperature threshold method in figures 3(*a*) and (*b*), respectively.

The crests detected by the two methods differ primarily near the outside edges. The crest-PIV fronts follow the location of the maximum temperature change while the fronts for the image-PIV method are the location of maximum

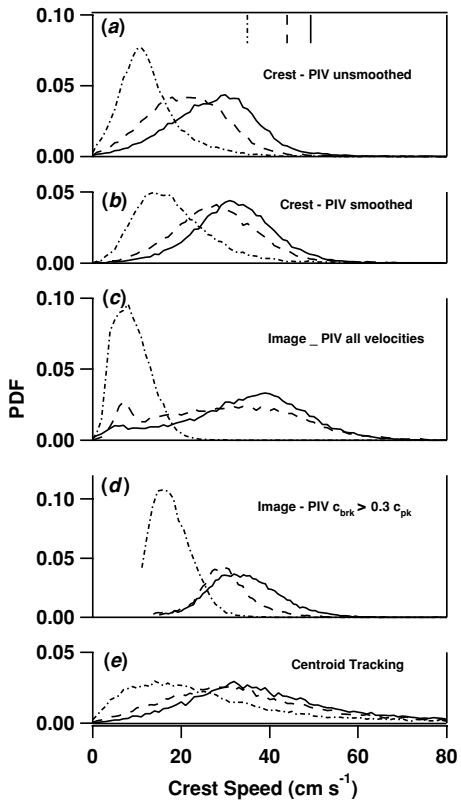

Figure 4. Probability distribution functions (PDFs) for breaking front velocities estimated using (*a*) crest-PIV without smoothing, (*b*) crest-PIV after smoothing, (*c*) image-PIV using all identified velocity vectors, (*d*) image-PIV using the criterion $c_{\mathrm{brk}} > 0.3c_{\mathrm{pk}}$, and (*e*) centroid tracking. The legend is the same as figure 1.

velocity. That these locations differ at the edges implies that the maximum velocity is not necessarily coincident with the temperature front that heretofore has been taken as the location of the crest. This result is surprising considering the results reported by Zappa *et al* [9], who used overlapping IR and optical slope imagery. They found that the leading edge of thresholded wakes in the IR imagery corresponded to crests in the slope imagery. However, the location of the wake outline in the IR image is, by definition, dependent on the threshold and thus will not necessarily coincide with the maximum velocity. For both crest velocity methods, a mean velocity vector was associated with each wave crest by averaging the individual velocity vectors along the crest. The mean velocity probability density functions (PDFs) for both methods are shown in figures 4(*a*)–(*c*). The value of c_{pk} for each wind speed is indicated by the vertical lines along the top axis and the ratio $c_{\mathrm{br}}/c_{\mathrm{pk}}$ is listed in table 2.

This ratio ranges from 0.31 to 0.70, depending on the method used, and indicates that the majority of breaking crests move at a speed that is less than the dominant wave speed. A ratio significantly less than unity could imply that waves of much shorter wavelength than the dominant waves are breaking. This implication is physically unreasonable for the narrowband spectrum in the laboratory. A possible explanation for the relatively low value of $c_{\mathrm{brk}}/c_{\mathrm{pk}}$ is the variation in speed along the length of the crest. Breaking crests are generally curved, implying that the velocity at the centre is greater than the velocity along the edges. The value of c_{brk} used in the

Table 2. Ratio of c_{brk}/c_{pk} for the crest-PIV, image-PIV and the centroid tracking method as a function of wind speed. The crest-PIV methods are further divided into an unsmooth and a smooth method and the unsmooth method has ratios for two different subtended angles of $\pm 90^\circ$ and $\pm 45^\circ$ from the centroid to define the crest. The image-PIV method shows ratios based on distributions comprising all the velocities and only those greater than $0.3c_{pk}$.

	c_{brk}/c_{pk}					
	Crest-PIV			Image-PIV		Centroid tracking
	Unsmooth					
Wind speed (m s^{-1})	$\pm 90^\circ$	$\pm 45^\circ$	Smooth	All velocities	$0.3c_{pk}$	
6.2	0.31	0.54	0.4	0.22	0.43	0.4
8.1	0.44	0.85	0.622	0.56	0.64	0.69
9.6	0.61	0.85	0.63	0.62	0.63	0.65

distributions is the mean of the velocities along the entire length of the detected crest. Therefore, the mean used in the distribution should be less than the maximum at the centre when the crest is curved.

This explanation is supported by recomputing the distributions using a smaller subtended angle to define the length over which the velocity is averaged. As listed in table 2 for the unsmoothed crest-PIV method, the ratio c_{brk}/c_{pk} for a subtended angle of $\pm 90^\circ$ ranged from 0.31 to 0.61, while for an angle of $\pm 45^\circ$ the ratio ranged from 0.54 to 0.85. The increase in the ratio for the shorter crests emphasizes the importance of the definition of the crest length on crest speed. By defining c_{brk} as the mean of the velocity along the crest, the ratio c_{brk}/c_{pk} is dependent on the extent of the crest specified by the detection algorithm. Alternative approaches include using the maximum velocity along the crest or using a very narrow angle to define the velocity and a wider angle to define the length. A thorough investigation to determine the most appropriate definition for the crest length and velocity will require a more extensive data set than we have at this time and is thus beyond the scope of this paper.

For both methods, the peak velocity increases with wind speed, which is expected since c_{pk} also increases with wind speed. The PDFs for the unsmoothed and smoothed crest-PIV method are similar in that their peak frequencies are comparable. Differences are seen in the density magnitudes at the lower velocities and most clearly for the lowest wind speed, where in the smooth case the peak is reduced and the distribution broadened. The PDF for the image-PIV method in figure 4(*c*) is similar to the PDFs for the crest-PIV methods in figures 4(*a*) and (*b*) for large velocities but show increased values at lower velocities. This result suggests that the PDFs for the image-PIV method include slower velocities that are not associated with breaking crests.

As described above, the distribution of velocities for the image-PIV method was determined by extracting the maximum velocities along the length of unsmoothed crests identified by the temperature threshold. This approach suggests two possible sources of slower velocities. First, the slower velocities may be associated with the outside edges of the crests, where the crest slows down. The outside edge of the crest is determined by the definition of the crest length based on the subtended angle of $\pm 90^\circ$ from the wake centroid, as described above. A second possibility is that the velocity extraction method may be associating velocities with features in the ROIs from the temperature thresholding that are not actively breaking crests.

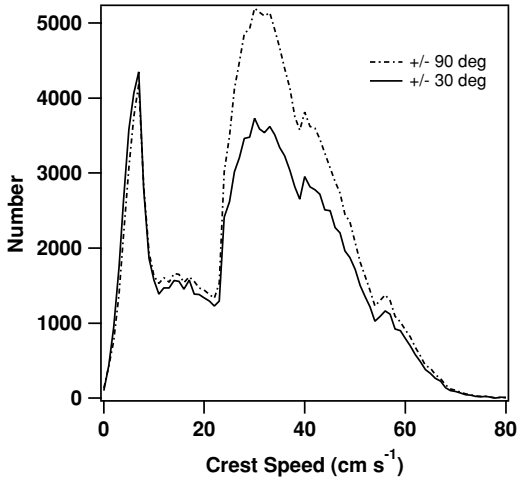

Figure 5. Histogram of crest velocities prior to averaging using $\pm 90^\circ$ and $\pm 30^\circ$ as the subtended angles to determine the breaking wave fronts.

To determine if the edges of the crests are the source of the slower velocities, we reduced the subtended angle to $\pm 30^\circ$ and examined the histogram of the individual velocity vectors, before averaging across the crest lengths. The result of this exercise for the highest wind speed is given in figure 5, which shows the histogram of the individual velocity vectors for the subtended angles of $\pm 30^\circ$ and $\pm 90^\circ$. The distributions are clearly bimodal, with the higher peak being associated with breaking crests and the lower peak likely associated with slower-moving, non-breaking features. Changing the subtended angle reduced the higher peak but had a negligible effect on the lower peak. This result suggests that the source of the slower velocities is not associated with reduced speed at the outside edges of the crests.

The fact that the lower velocity peak does not change with the subtended angle implies that the slower velocities are indeed associated with slower moving, non-breaking features. A likely source of the slower velocities is from crests detected by the threshold method that are near the end of the breaking process, as the crest slows down. The bimodal nature of the distribution of the velocities in figure 5 suggests that a velocity threshold can be used to eliminate the slower velocities not associated with actively breaking crests. Based on inspection of the velocity histograms for all wind speeds, a velocity threshold of $0.3c_{pk}$ was applied to the individual velocities from the image-PIV method and the PDF of the average crest

velocities was recomputed. The resulting PDFs in figure 4(*d*) now show single peaks that are similar to the PDFs for the threshold-based methods in figures 4(*a*) and (*b*). However, the peaks in the image-PIV distributions are significantly narrower than those in the crest-PIV distributions. This narrowing of the distributions is consistent with the notion that the crest-PIV distributions include slower velocities not associated with actively breaking crests. That these slower velocities are due to crests being detected by the temperature threshold after they have slowed down implies that the results are dependent on the threshold level used. This emphasizes the disadvantage of detecting the breaking crests based on the temperature. On the basis of this result and the appearance of the velocity maps, we would judge the image-PIV distributions to be superior to those of the crest-PIV method.

However, unlike the crest-PIV method, we find that the ratio $c_{\mathrm{brk}}/c_{\mathrm{pk}}$ remains relatively low compared to unity when the subtended angle is reduced. This result is not surprising since the crests detected in the image-PIV method are relatively straight (see figure 3(*c*)). As explained above, the crests are defined by the location of the maximum velocity along the horizontal direction within the ROI containing the crests detected using the temperature threshold. The relatively low value of $c_{\mathrm{brk}}/c_{\mathrm{pk}}$ is likely an indication of the fact that the velocities from the image-PIV algorithm are an average over the finite area of the window size. This is in contrast to the crest-PIV method that gives the velocity of the detected crest, which is typically a few pixels wide. The implication that the crest velocity is underestimated is a significant disadvantage of the image-PIV method over the crest-PIV method.

In order to independently judge the distributions derived using the PIV-based techniques, a method was developed to derive an estimate of the crest velocities by tracking individual events. Individual breaking crests were identified and then tracked in time as they propagated down the image. An estimate of the crest velocity was computed from the displacement of the centroid of the crest as it propagated through the field-of-view. Figure 6 shows the time history of tracking an individual crest by showing successive crests and their centroids. The PDFs of the crest velocities using the centroid-tracking method are shown in figure 4(*e*). The peak velocities of the PDFs in figure 4(*e*) are comparable to those in figures 4(*a*)–(*d*) but they are much broader. The broadening of the peaks is likely caused by basing the velocity on the motion of the centroid, which has an averaging effect. Nonetheless, the consistency of the peaks between the centroid tracking method and both the crest-PIV and image-PIV methods supports the validity of the PIV-based approach.

5. Crest length distribution and turnover rate

In order to compute the distribution $\Lambda(c)$, a crest length and average velocity is computed for each crest. Based on the definition by Phillips [1], the distribution is given by

$$\Lambda(c) = \frac{\sum_{c\in|c,c+\mathrm{d}c|} L_i}{A_{\mathrm{s}}} \qquad (3)$$

where L_i is the length of the ith crest in the speed interval c to $c + \mathrm{d}c$ and A_{s} is the area of the image. The summation is performed for all detected events in the imaged area.

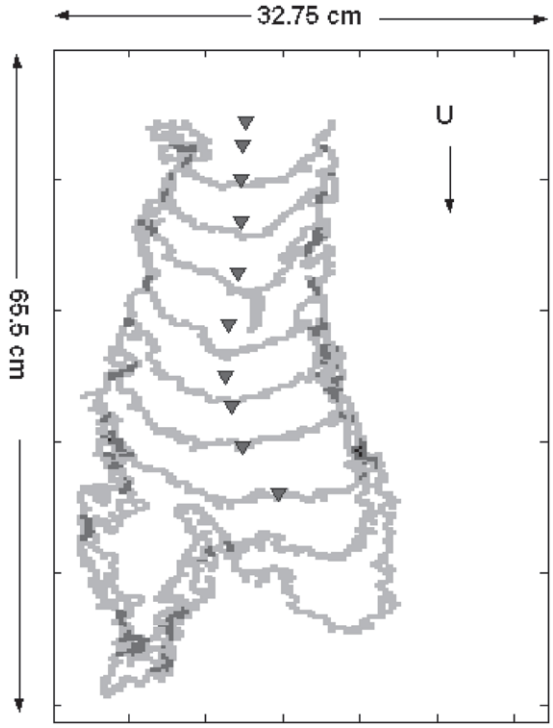

Figure 6. Crest tracking sequence where multiple crests tracked over the lifetime of a single breaking wave have been overlaid to form one image. Downwards pointing triangles show the movement of the centroid of the wake as the breaking wave front propagates.

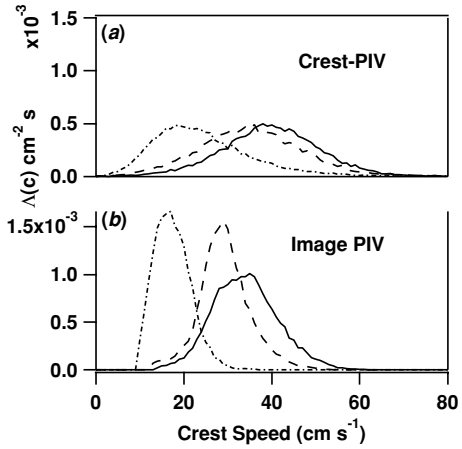

Figure 7. Distribution $\Lambda(c)$ for three wind speeds using (*a*) the crest-PIV technique with the smoothing and (*b*) the image-PIV technique. The legend is the same as figure 1.

Subsequent moments of $\Lambda(c)$ are computed by multiplying (3) by c^n, at the respective intervals, where n corresponds to the nth moment.

The $\Lambda(c)$ distribution can be thought of as a combination of the length and velocity histograms. The distribution is built up by sorting the detected crests by velocity and summing up the lengths in each velocity bin. The resulting $\Lambda(c)$ distribution for both the crest-PIV and the image-PIV methods is shown in figure 7. The distributions are similar in shape and offset to the corresponding velocity PDFs in figures 4(*b*) and (*d*). The image-PIV distributions are narrower and more separated than those of the crest-PIV method.

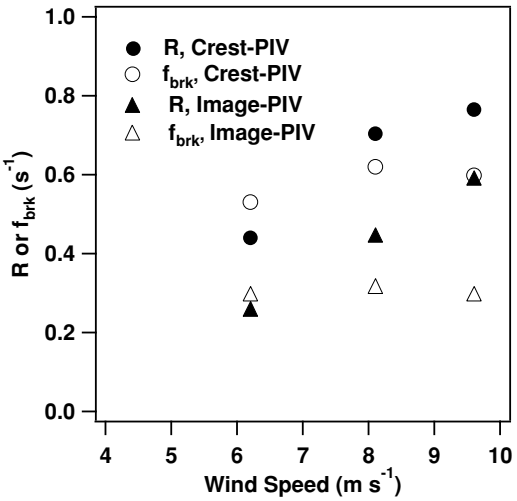

Figure 8. Turnover rate, R, or frequency of breaking, $f_{\rm brk}$ (s^{-1}), versus wind speed. Solid symbols are for R computed using (1) and open symbols are for $f_{\rm brk}$ computed using (4). Circles indicate values computed using crest-PIV with smoothing and triangles indicate values estimated using the image-PIV technique.

The turnover rates given by (1) for both the crest-PIV (smooth) and the image-PIV methods are plotted versus wind speed as solid symbols in figure 8. The turnover rate increases with wind speed and the dependence on wind speed for each case is similar. The values for the crest-PIV method are larger than those for the image-PIV method, which is consistent with the observation that the measured crest lengths are less for the image-PIV method (e.g., compare figures 3(b) and (c)). The difference between the two methods emphasizes the importance of the crest length in determining derived quantities. The magnitude of the turnover rate for the image-PIV method ranges from roughly 0.2 Hz at the low wind speed to 0.5 Hz at the high wind speed, implying that 20% to 50% of the surface is turned over every second.

The turnover rate given by (1) should be equivalent to the breaking wave frequency, defined by Phillips [1] as the total number of breaking waves passing a given point per unit time. The equivalence can be demonstrated by considering each pixel in the image as a virtual wave probe and taking the average of the number of waves passing each pixel for a given duration. For the ith pixel, we define a binary variable p_i, where $p_i = 1$ if a breaking crest is present and $p_i = 0$ otherwise. For a sequence of N images consisting of M pixels per image, the frequency of breaking, $f_{\rm brk}$, is given by

$$f_{\rm brk} = \frac{f_{\rm s}}{MN} \sum_{j=0}^{M-1} \left(\sum_{i=0}^{N-1} p_i \right)_j , \qquad (4)$$

where $f_{\rm s}$ is the image sample frequency. This equation can be interpreted as the average value of the frequency of breaking for the M points in the image over a time interval of $N/f_{\rm s}$. The result of applying (4) to the crests determined by the crest-PIV (smooth) and the image-PIV methods is plotted in figure 8 as open circles. In general, the values of $f_{\rm brk}$ for each method are close to the corresponding values of R. However, $f_{\rm brk}$ decreases for the highest wind speed. The most likely cause of this is the fact that the crests are only one pixel wide. If a crest moves farther than one pixel during the time between frames, then the measured frequency of breaking would be less than the actual value. A further complication is that the shape of a given crest may change by several pixels from one frame to the next, which could also affect the frequency of breaking calculation. Our initial attempts to develop a robust algorithm to calculate the frequency of breaking indicate that the best approach is to track individual events in order to calculate the area swept out by the crest as it propagates. This is the subject of ongoing research and will be reported on in the future. For the purposes of this study, we conclude that the order of magnitude of the turnover rate given by (1) is comparable to the frequency of breaking.

6. Summary and conclusion

Infrared imagery was used to investigate the geometric and kinematic properties for microscale breaking waves. Image processing algorithms were developed to provide estimates of $\Lambda(c)$, the distribution of breaking crest lengths as a function of crest speed, in a laboratory wind–wave tank. To the best of our knowledge, this is the first report of $\Lambda(c)$ for microbreaking.

Two methods based on applying a standard PIV algorithm to the IR imagery were developed. In the crest-PIV method, velocities were estimated by applying the PIV algorithm to binary images of crests detected using a temperature threshold. The crest-PIV method was applied to unsmoothed and smoothed crests detected using a temperature threshold. In the image-PIV method, the PIV algorithm was applied to the unprocessed IR images and resulted in a velocity map covering each entire image. Crest velocities and lengths were extracted from the velocity map by locating the maximum velocity in a region of interest based on the crest location from the temperature thresholding technique.

The crest-PIV method tended to produce spurious vectors near the ends of the crest lengths. In contrast, the image-PIV method produced a velocity map with very few spurious vectors. A notable result is that the maximum crest velocity is not necessarily coincident with the location of the wake defined by the temperature threshold. The advantages of the image-PIV method over the crest-PIV method are the smoother appearance of the velocity maps and that it uses a velocity threshold based on the crest speed of the dominant wave. The crest-PIV method is based on a temperature threshold that is determined empirically. However, the image-PIV method was found to underestimate the crest velocity based on the change in the ratio $c_{\rm brk}/c_{\rm pk}$, when the crest length was reduced. The turnover rate computed from (1) based on the measured $\Lambda(c)$ was comparable to the frequency of breaking given by (4) and based on the detected crests.

The amount of data and the range of conditions available for this study were not sufficient to investigate the application of $\Lambda(c)$ to issues of heat and momentum flux via (1) and (2). Furthermore, application of the method to the field will likely require refinement because the surface displacement spectrum in the laboratory is narrow compared to that in the field. Nonetheless, the results of the algorithms developed demonstrate that IR techniques can be used to estimate $\Lambda(c)$ for microbreaking waves. The results suggest that application of the techniques developed here to a larger and more varied data set will provide significant advancement of our knowledge of the role of microscale breaking waves in air–sea fluxes.

Acknowledgments

This work was supported by grants from the Office of Naval Research and the National Science Foundation. We thank Mohamed Atmane for assistance in the experiment and with development of the PIV algorithm.

References

[1] Phillips O M 1985 Spectral and statistical properties of the equilibrium range in wind-generated gravity waves *J. Fluid Mech.* **156** 505–31

[2] Hara T and Belcher S 2002 Wind forcing in the equilibrium range of wind-wave spectra *J. Fluid. Mech.* **470** 223–45

[3] Phillips O, Posner F and Hansen J 2001 High range resolution radar measurements of the speed distribution of breaking events in wind-generated ocean waves: surface impulse and wave energy dissipation rates *J. Phys. Ocean.* **31** 450–60

[4] Melville W K and Matusov P 2002 Distribution of breaking waves at the ocean surface *Nature* **417** 58–63

[5] Duncan J H 1981 An experimental investigation of breaking waves produced by a towed hydrofoil *Proc. R. Soc.* A **377** 331–48

[6] Banner M L and Phillips O M 1974 On the incipient breaking of small scale waves *J. Fluid Mech.* **65** 647–56

[7] Katsaros K 1980 The aqueous thermal boundary layer *Bound.-Layer Meteorol.* **18** 107–27

[8] Jessup A, Zappa C and Yeh H 1997 Defining and quantifying microscale breaking with infrared imagery *J. Geophys. Res.* **102** 23145–53

[9] Zappa C, Asher W and Jessup A 2001 Microscale wave breaking and air-water gas transfer *J. Geophys. Res.* **106** 9385–91

[10] Jessup A *et al* 1997 Infrared remote sensing of breaking waves *Nature* **385** 52–5

[11] Siddiqui M *et al* 2001 Simultaneous particle image velocimetry and infrared imagery of microscale breaking waves *Phys. Fluids* **13** 1891–903

[12] Siddiqui M *et al* 2004 Coherent structures beneath wind waves and their influence on air-water gas transfer *J. Geophys. Res.* **109** C03024

[13] Volino R J and Smith G 1999 Use of simultaneous IR temperature measurements and DPIV to investigate thermal plumes in a thick layer cooled from above *Exp. Fluids* **27** 70–8

[14] Zhang X and Harrison S 2004 A laboratory observation of the surface temperature and velocity distribution on a wavy and windy air-water interface *Phys. Fluids* **16** L5–8

[15] Phadnis K R 2004 *The Distribution of Microscale Breaking Waves in a Wind Wave Tank* (Seattle, WA: University of Washington) p 122

[16] Siddiqui K 2002 *Laboratory Measurements of the Flow Beneath Microscale Breaking Waves* (University of Toronto) p 183

[17] Atmane M, Asher W and Jessup A 2004 On the use of the active infrared technique to infer heat and gas transfer velocities at the air–water free surface *J. Geophys. Res.* **109** 15

[18] Willert C and Gharib M 1991 Digital particle image velocimetry *Exp. Fluids.* **10** 181–93